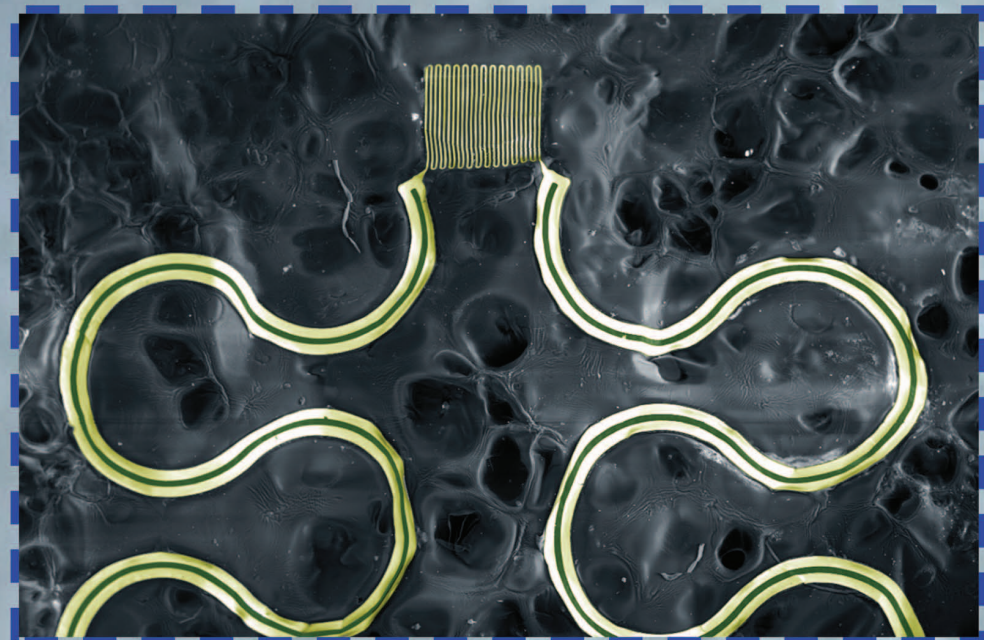


ADVANCED HEALTHCARE MATERIALS



Theoretical and Experimental Studies of Epidermal Heat Flux Sensors for Measurements of Core Body Temperature

Yihui Zhang, Richard Chad Webb, Hongying Luo, Yeguang Xue, Jonas Kurniawan, Nam Heon Cho, Siddharth Krishnan, Yuhang Li, Yonggang Huang, and John A. Rogers*

Long-term, continuous measurement of core body temperature is of high interest, due to the widespread use of this parameter as a key biomedical signal for clinical judgment and patient management. Traditional approaches rely on devices or instruments in rigid and planar forms, not readily amenable to intimate or conformable integration with soft, curvilinear, time-dynamic, surfaces of the skin. Here, materials and mechanics designs for differential temperature sensors are presented which can attach softly and reversibly onto the skin surface, and also sustain high levels of deformation (e.g., bending, twisting, and stretching). A theoretical approach, together with a modeling algorithm, yields core body temperature from multiple differential measurements from temperature sensors separated by different effective distances from the skin. The sensitivity, accuracy, and response time are analyzed by finite element analyses (FEA) to provide guidelines for relationships between sensor design and performance. Four sets of experiments on multiple devices with different dimensions and under different convection conditions illustrate the key features of the technology and the analysis approach. Finally, results indicate that thermally insulating materials with cellular structures offer advantages in reducing the response time and increasing the accuracy, while improving the mechanics and breathability.

body temperature is a critical index for monitoring health status.^[2,3] Previous approaches/devices developed for measuring the core body temperature fall into two main groups: 1) invasive approaches^[4–7] that involve sensors inserted into a natural body cavity, such as an ingestible or implanted telemetric device; 2) noninvasive approaches^[8–13] that quantify core body temperature indirectly from measurements of skin temperature and heat flow, such as the zero-heat-flow^[8–11] and the dual-heat-flux methods.^[12,13] Invasive approaches offer excellent accuracy, but they have obvious disadvantages in discomfort and risk of complications. Noninvasive approaches are, as a result, of widespread interest. Devices/instruments of this type have been used in cardiac surgery and in monitoring of circulatory failure.^[14] The rigid, planar formats of these devices, however, do not allow natural or comfortable integration with soft, curvilinear surfaces of the skin. The consequences range from

irritation to the skin to thermal and mechanical loading of its surface, thereby degrading the measurement fidelity and frustrating use in continuous monitoring.

Here, we introduce an approach and a set of materials for noninvasive measurement of core body temperature, in which multiple mechanically compliant differential temperature sensors attach softly, intimately, and naturally onto the surface of skin. The scheme takes advantage of multiple (e.g., 8) temperature readings from a

1. Introduction

Core body temperature is an important parameter in guiding clinical decisions in patient care. A substantial deviation from normal temperature indicates a risk of organ dysfunction and a serious threat to a patient's health.^[1] In particular, for patients suffering from traumatic brain injury or nerve damage, core

Dr. Y. Zhang, H. Luo, Y. Xue, Dr. Y. Li, Prof. Y. Huang
Departments of Civil and Environmental Engineering
and Mechanical Engineering
Center for Engineering and Health
and Skin Disease Research Center
Northwestern University
Evanston, IL 60208, USA

Dr. Y. Zhang
Center for Mechanics and Materials
Tsinghua University
Beijing 100084, China

R. C. Webb, J. Kurniawan, N. H. Cho, S. Krishnan
Department of Materials Science and Engineering
Frederick Seitz Materials Research Laboratory
University of Illinois at Urbana-Champaign
Urbana, IL 61801, USA

H. Luo
School of Aerospace Engineering and Applied Mechanics
Tongji University
Shanghai 200092, China

Dr. Y. Li
Institute of Solid Mechanics
Beihang University
Beijing 100191, China

Prof. J. A. Rogers
Department of Materials Science and Engineering
Chemistry
Mechanical Science and Engineering
Electrical and Computer Engineering
Beckman Institute for Advanced Science and
Technology and Frederick Seitz Materials Research Laboratory
University of Illinois at Urbana-Champaign
Urbana, IL 61801, USA
E-mail: jrogers@illinois.edu



DOI: 10.1002/adhm.201500110

collection of sensors to enhance the accuracy. The device exploits advanced structural designs^[15–24] recently developed for stretchable electronics to allow low effective moduli and large strain deformations.^[18,25–34] Various aspects of the approach, including the sensitivity, accuracy, and response time, can be revealed through the use of finite element analyses (FEA). Further experiments illustrate that the device can offer not only accurate assessments of core body temperature over a wide range, but also capabilities in identifying the convective properties of the surrounding air.

2. Results

2.1. Device Design and Mechanical Characteristics

As elaborated by the theoretical models described in the following subsections, the core body temperature can be

determined indirectly through use of multiple differential temperature sensors. Each differential temperature sensor adopts a multilayer design as in **Figure 1a**. Two identical sensors separated by a soft (e.g., 200 kPa) layer of silicone utilize the temperature coefficient of resistance in thin (100 nm), narrow (10 μm) serpentine traces of gold to offer high precision (on the order of millikelvin) measurements.^[35] Both sensors are linked by electrical interconnects (Ti/Cu/Ti/Au; 50 μm wide and 600 nm thick) in a filamentary serpentine mesh for direct external addressing. Interconnects provide a four-point measurement configuration to minimize errors associated with contact resistances. These metallic interconnects lie between two thin layers of polyimide (PI) of the same thickness (1.2 μm) to minimize the strain in the metal by placing it at the neutral mechanical plane. Two thin (e.g., 50 μm) silicone layers encapsulate the entire device to avoid

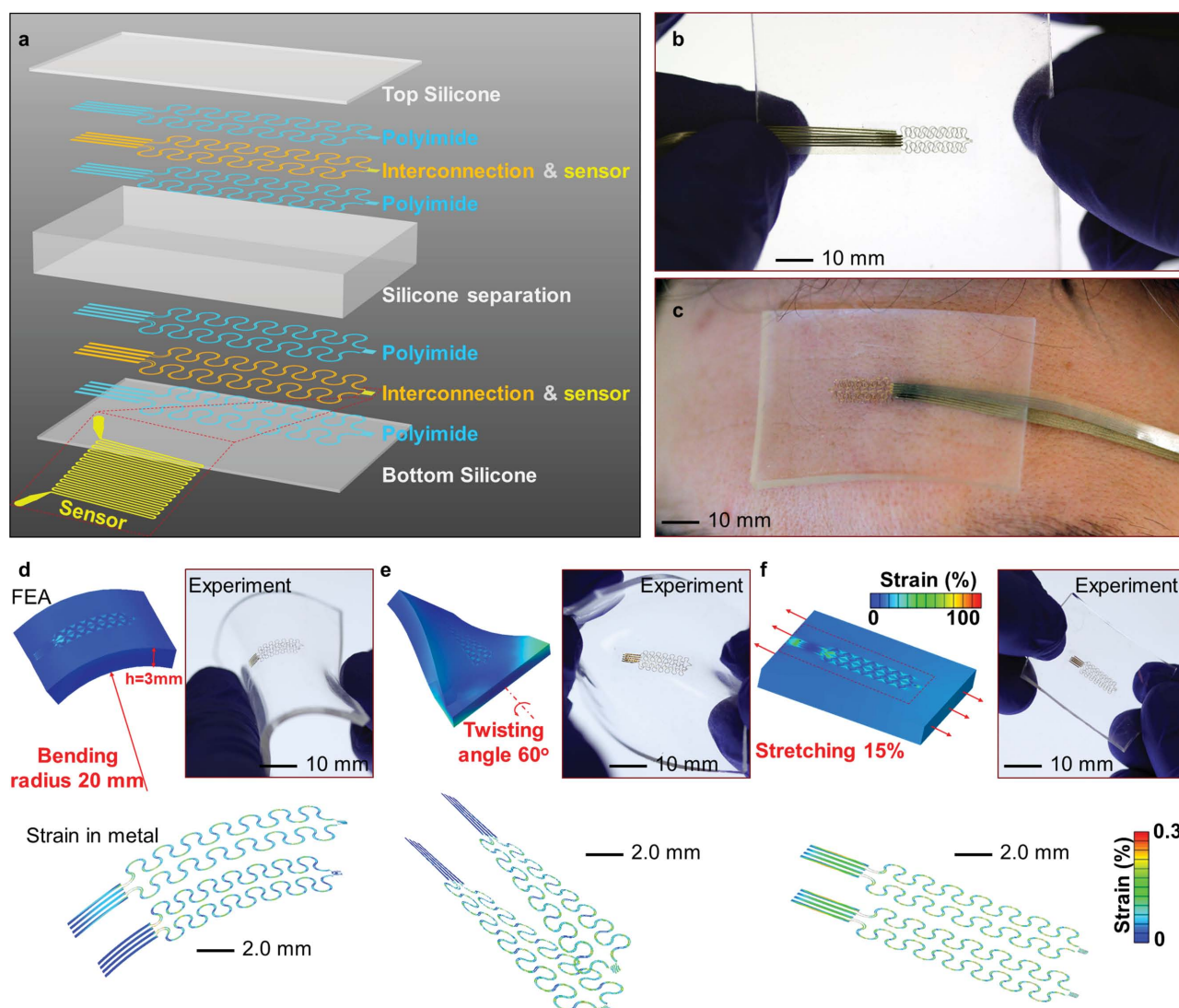


Figure 1. Device construction and mechanics under deformation. a) Schematic illustration of the device layout in an exploded view. Optical images of a device b) held in the hands and c) mounted on the forehead; FEA results and optical image of a device subject to d) bending to a radius of curvature of 20 mm, e) twisting at an angle of 60°, and f) uniaxial stretching to a strain of 15%. The color in the FEA results represents the magnitude of logarithmic strains in the silicone and metal.

direct exposure to the environment. Figure 1b presents an optical image of such a device fabricated using microlithographic techniques (see the Experimental Section for details). Conformal attachment to the skin in all cases occurs with the use of an ultrathin (e.g., 40 μm) elastomer layer (e.g., Silbione RT Gel 4147 A/B, Bluestar Silicones, USA; modulus ≈ 3 kPa), even for the thickest device geometries (e.g., 5.9 mm). An example appears in Figure 1c, showing a thick (3.0 mm) device well attached to the forehead. The effective modulus of the system reduces slightly (from ≈ 216 to ≈ 202 kPa) with increasing device thickness from 0.5 to 6.0 mm (Figure S1, Supporting Information). All values are comparable to that of the human epidermis, thereby yielding a type of conformable integration that poses negligible mechanical loading on the skin surface, as opposed to rigid devices. The concurrent use of the serpentine mesh design, the neutral mechanical plane construction, and the ultrasoft substrate yields highly deformable characteristics and minimized material strain in the interconnects and sensors. For example, 3D FEA calculations (see the Supporting Information for details) show that the strain in the metal just reaches the yield strain ($\approx 0.3\%$) upon bending on a rigid cylinder with a radius of ≈ 20 mm (as shown in Figure 1d). Furthermore, the device can be twisted by $\approx 60^\circ$ (Figure 1e) or stretched by $\approx 15\%$ (Figure 1f), in elastic and reversible manners, through microscale wrinkling of the serpentine traces. In all cases (Figure 1d–f), the deformation modes in the experiment are similar to those in FEA results, and no cracks or failures are observed. These superior mechanical attributes facilitate use on the skin, and well accommodate natural motions, for which strains are typically below $\approx 15\%$.

2.2. Theoretical Model and Sensitivity Analyses

A theoretical model of heat conduction can be used to extract the core body temperature using data from multiple differential temperature sensors with various separation thicknesses. For each device, when the lateral sizes are much larger than the thicknesses (e.g., 20 mm \times 20 mm \times 1 mm), the heat flux mainly occurs along the thickness direction, as schematically illustrated in Figure 2a. In this case, the 1D heat conduction can be adopted such that the temperature (T) is governed by the equation $\partial^2 T / \partial z^2 = 0$, where z denotes the coordinate along the thickness direction. Theoretically, the temperature at the skin surface is mainly determined by the core body temperature, through the effective thermal properties of the tissues and the ambient conditions. The heterogeneous construction of the tissue structures and associated temperature distributions within these areas are not critical. Based on this consideration, we assume that the skin and underlying tissues can be treated as an equivalent single-layer tissue (with an equivalent thickness t_{tissue} and thermal conductivity k_{tissue}). The bottom surface of the device remains in intimate contact with the equivalent tissue, while on its top, a thin fabric (with thickness t_{fabric} and thermal conductivity k_{fabric}) can be used in the experiment to model conditions of practical use. This fabric layer exchanges heat directly with the surrounding air

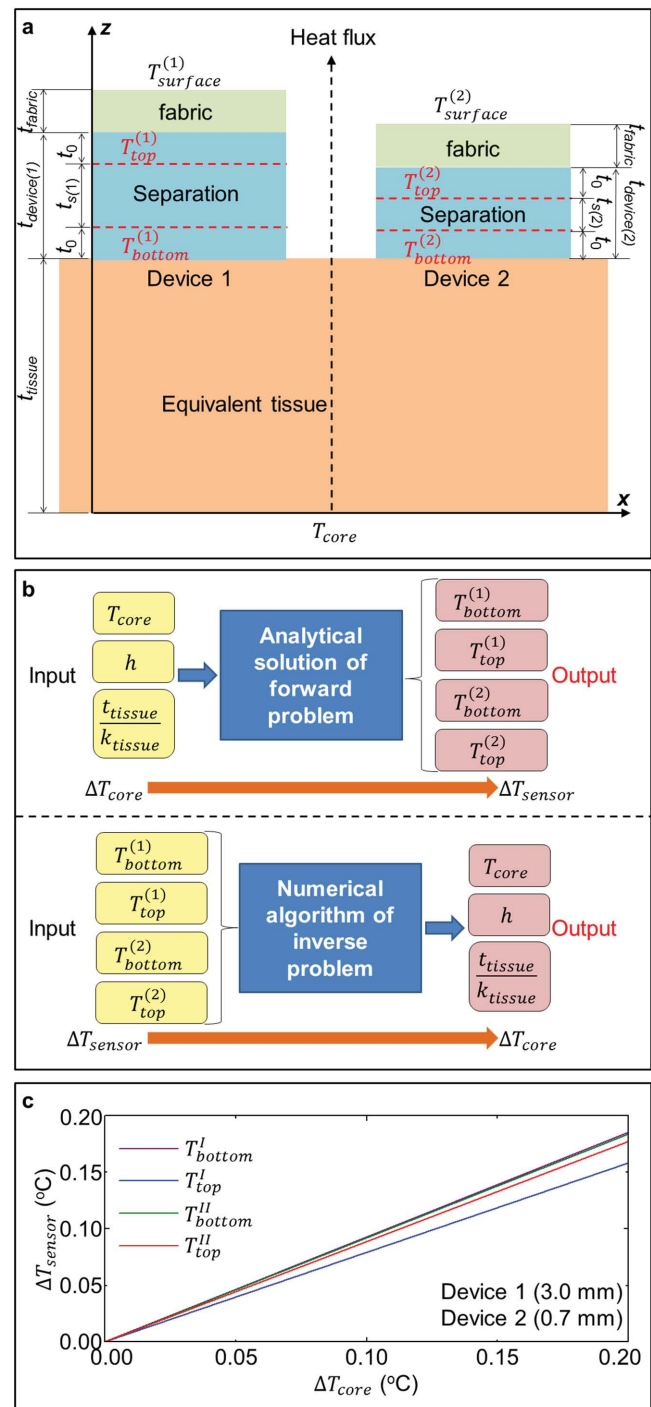


Figure 2. Illustration of the thermal conduction model and sensitivity analyses. a) Schematic illustration of the thermal conduction model. b) Illustration of the sensitivity in the forward problem (top panel) and the accuracy in the inverse problem (bottom panel). c) Variation of sensor temperatures versus changes in the core body temperature, for two different devices with $t_{\text{device}(1)} = 3.0$ mm, $t_{\text{device}(2)} = 0.7$ mm, $t_0 = 0.05$ mm, and $t_{\text{fabric}} = 1.0$ mm.

(T_{room}) through its free surface, with a convection coefficient of h . Taking device 1 as an example, the above boundary conditions can be expressed as

$$T_{\text{tissue}}|_{z=0} = T_{\text{core}} \quad (1a)$$

$$T_{\text{tissue}}|_{z=f_{\text{tissue}}} = T_{\text{device}(1)}|_{z=f_{\text{tissue}}}, \quad (1b)$$

$$\left[k_{\text{tissue}} \frac{dT_{\text{tissue}}}{dz} \right] \Big|_{z=f_{\text{tissue}}} = \left[k_{\text{silicone}} \frac{dT_{\text{device}(1)}}{dz} \right] \Big|_{z=f_{\text{tissue}}}$$

$$T_{\text{device}(1)}|_{z=f_{\text{tissue}}+f_{\text{device}(1)}} = T_{\text{fabric}}|_{z=f_{\text{tissue}}+f_{\text{device}(1)}} \quad (1c)$$

$$\left[k_{\text{silicone}} \frac{dT_{\text{device}(1)}}{dz} \right] \Big|_{z=f_{\text{tissue}}+f_{\text{device}(1)}} = \left[k_{\text{fabric}} \frac{dT_{\text{fabric}}}{dz} \right] \Big|_{z=f_{\text{tissue}}+f_{\text{device}(1)}}$$

$$\left[k_{\text{fabric}} \frac{dT_{\text{fabric}}}{dz} \right] \Big|_{z=f_{\text{tissue}}+f_{\text{device}(1)}+f_{\text{fabric}}} = -h(T_{\text{fabric}}|_{z=f_{\text{tissue}}+f_{\text{device}(1)}+f_{\text{fabric}}} - T_{\text{room}}) \quad (1d)$$

where the subscripts “tissue,” “device(1),” and “fabric” represent three different layers; $t_{\text{device}(1)} = 2t_0 + t_{s(1)}$, $t_{s(1)}$, and t_0 denote the thicknesses of entire device, separation layer, and encapsulation layer, respectively; k_{silicone} denotes the thermal conductivity of the silicone. Based on these boundary conditions and the heat conduction equation, the temperatures ($T_{\text{top}}^{(1)}, T_{\text{bottom}}^{(1)}$) of the two sensors in device 1 can be related to the core body temperature (T_{core}) by

$$T_{\text{top}}^{(1)} = T_{\text{room}} + \frac{T_{\text{core}} - T_{\text{room}}}{\frac{t_{\text{tissue}}}{k_{\text{tissue}}} + \frac{t_{\text{device}(1)}}{k_{\text{silicone}}} + \frac{t_{\text{fabric}}}{k_{\text{fabric}}} + \frac{1}{h}} \left(\frac{t_{\text{fabric}}}{k_{\text{fabric}}} + \frac{1}{h} + \frac{t_0}{k_{\text{silicone}}} \right) \quad (2)$$

$$T_{\text{bottom}}^{(1)} = T_{\text{room}} + \frac{T_{\text{core}} - T_{\text{room}}}{\frac{t_{\text{tissue}}}{k_{\text{tissue}}} + \frac{t_{\text{device}(1)}}{k_{\text{silicone}}} + \frac{t_{\text{fabric}}}{k_{\text{fabric}}} + \frac{1}{h}} \left(\frac{t_{\text{fabric}}}{k_{\text{fabric}}} + \frac{1}{h} + \frac{t_0 + t_{s(1)}}{k_{\text{silicone}}} \right) \quad (3)$$

The ambient temperature (T_{room}), which is required as an input into the models, can easily be obtained using a separate, conventional device exposed to the surrounding air, perhaps attached to a piece of clothing. The three unknown parameters to be determined in Equations (2) and (3) are the core body temperature (T_{core}), the equivalent tissue property ($t_{\text{tissue}}/k_{\text{tissue}}$), and the convection coefficient (h). These quantities cannot be determined directly from temperature data derived using just one differential temperature sensor. Two strategies to solve this issue use: i) multiple devices with different separation thicknesses (t_s); ii) multiple devices with different separation materials (and thereby different conductivities k_{silicone}). This section focuses on strategy (i) to illustrate the model implementation and experimental validation. Section 3 discusses an extension to strategy (ii).

Consider n (≥ 2) different differential devices with different separation thicknesses [$t_{s(1)}$ to $t_{s(n)}$] and the same encapsulation

thickness (t_0). Each device yields two temperature readings ($T_{\text{top}}^{(i)}, T_{\text{bottom}}^{(i)}$, $i = 1, \dots, n$), with a total of $(2n)$ equations, for the determination of the three unknowns ($T_{\text{core}}, t_{\text{tissue}}/k_{\text{tissue}}, h$). This inverse problem can be solved by constructing an objective functional (Π) that accounts for the relative error of each equation, which reads

$$\Pi(T_{\text{core}}, t_{\text{tissue}}/k_{\text{tissue}}, h) = \sum_{i=1}^n \left[\frac{T_{\text{core}} - T_{\text{room}}}{T_{\text{top}}^{(i)} - T_{\text{room}}} \frac{\frac{t_{\text{fabric}}}{k_{\text{fabric}}} + \frac{1}{h} + \frac{t_0}{k_{\text{silicone}}}}{\frac{t_{\text{tissue}}}{k_{\text{tissue}}} + \frac{t_{\text{device}(i)}}{k_{\text{silicone}}} + \frac{t_{\text{fabric}}}{k_{\text{fabric}}} + \frac{1}{h}} - 1 \right]^2 + \sum_{i=1}^n \left[\frac{T_{\text{core}} - T_{\text{room}}}{T_{\text{bottom}}^{(i)} - T_{\text{room}}} \frac{\frac{t_{\text{fabric}}}{k_{\text{fabric}}} + \frac{1}{h} + \frac{t_0 + t_{s(i)}}{k_{\text{silicone}}}}{\frac{t_{\text{tissue}}}{k_{\text{tissue}}} + \frac{t_{\text{device}(i)}}{k_{\text{silicone}}} + \frac{t_{\text{fabric}}}{k_{\text{fabric}}} + \frac{1}{h}} - 1 \right]^2 \quad (4)$$

Minimization of this functional by searching over a reasonable range for each parameter (see the Supporting Information for details) then gives solutions for the three unknowns. The process can be implemented numerically (e.g., using commercial software MATLAB or FORTRAN). Although biological activity (e.g., blood circulation) in regions beneath the skin may change the properties/parameters of the tissues, the theoretical models remain valid since they do not require these properties/parameters to be constant or separately known.

The sensitivity and accuracy are determined not only by the theoretical model, but also by the accuracy of the sensors. The sensitivity can be interpreted as the smallest level of change in the core body temperature that is detectable, as illustrated in the top panel of Figure 2b. According to Equations (2) and (3), the change in core body temperature induces a proportional change in the temperature of the two sensors in each device, through a factor that only depends on the various material and geometric parameters. For two representative devices (3.0 mm and 0.7 mm in thickness) under a typical convection condition ($h = 10 \text{ W m}^{-2} \text{ K}^{-1}$), the results in Figure 2c clearly show that a unit change (1.0 K) in the core body temperature leads to a $>0.7 \text{ K}$ change in all four sensors. According to Webb et al.^[35] temperature sensors with construction similar to those reported here can provide a precision (one standard deviation) of $\approx 14 \text{ mK}$, resulting in sensitivities of the current core body temperature system of $\approx 20 \text{ mK}$. On the other hand, the accuracy can be interpreted as the average error of prediction in the core body temperature caused by errors in the temperature sensors and the numerical algorithms, as illustrated in the bottom panel of Figure 2b. Calculations based on two representative devices (3.0 mm and 0.7 mm in thickness) show that an error in the measured temperature can be magnified by a factor of ≈ 5.2 in the prediction of core body temperature (Figure S2, Supporting Information). Use of additional devices can improve the accuracy of the prediction (Figure S3, Supporting Information). For example, the magnification factor of the average error in prediction can be reduced from ≈ 5.2 to ≈ 2.5 (Figure S4, Supporting Information), when the number of devices increases from 2 to 4. When the number of devices increases further to ≈ 12 , the magnification factor reaches ≈ 1.0 . Considering practical

limits, we mainly focused on four or fewer devices (typically with a lateral dimension of 20 mm × 20 mm) in this study. In practical use, the primary sources of sensor accuracy error are resistance changes resulting from deformation strain, and errors resulting from the measurement electronics. Analysis of resistance changes due to strain in similar devices^[35] reveals potential strain-induced accuracy errors of ≈100 mK under significant deformation. Potential drift in the accuracy of measurement electronics increases with the time since calibration. Drift errors resulting from the measurement electronics, 90 d after sensor calibration, can be expected to be as high as 250 mK for the configurations used here. The resultant average accuracy error in the determination of core body temperature with four devices (eight total sensors), due to the accuracy scaling, becomes 250–875 mK, depending on the time since calibration. The practical impact of these accuracy errors is diminished in use cases where the goal is to monitor continuous changes in the core body temperature over time. Here, the primary concern is precision, as opposed to absolute accuracy. Many examples of this type of use case exist, often in clinical settings, such as monitoring infant temperatures in incubators, or general patient temperature changes over time.

2.3. Effects of Transient and 3D Heat Conduction

The theoretical model described above uses steady-state heat conduction and assumes that the entire system is in an equilibrium state. When the core body temperature changes, the differential temperature device requires a certain time (i.e., the response time) to stabilize, determined mainly by the

thickness, diffusivity, and conductivity of the various layers. For a typical thickness (9.2 mm) and material parameters (thermal conductivity $k_{\text{tissue}} = 0.3 \text{ W m}^{-1} \text{ K}^{-1}$, heat capacity $c_{\text{tissue}} = 1460 \text{ J kg}^{-1} \text{ K}^{-1}$, and density $\rho_{\text{tissue}} = 970 \text{ kg m}^{-3}$) of the equivalent tissue layer, the transient FEA (see the Supporting Information for details) gives the temperature history (Figure 3a–d) of the top and bottom sensors for four devices with different thicknesses in response to the increase of core body temperature from 37 °C to 39 °C. These results on the temporal variations in temperature agree reasonably well with experimental measurement over the entire time range for the four different thicknesses (Figure S5, Supporting Information). The relatively large response time observed in the experiment can mainly be attributed to the different heating conditions used in the experiment and transient FEA, as evidenced by the slower stabilization in the experimentally controlled core body temperature. By defining the response time as that required to reach 90% of the final temperature change for both sensors in the device, FEA results indicate an increase in the response time from ≈474 s for the thinnest (0.67 mm) device to ≈1030 s for the thickest (5.90 mm) device. A numerical experiment that involves use of all of these time-dependent sensor temperatures (Figure 3a–d) in the inverse model gives time-dependent estimates for the core body temperature, the tissue property, and the convection coefficient, as shown in Figure 3e,f. The response time of the core body temperature is mainly limited by the thickest device and can be even larger (≈1440 s in this case), since a small error in the sensor temperature can be magnified to a certain extent in the inverse problem. Therefore, it is important to appropriately reduce the device thickness to provide fast responses to changes in core body temperature.

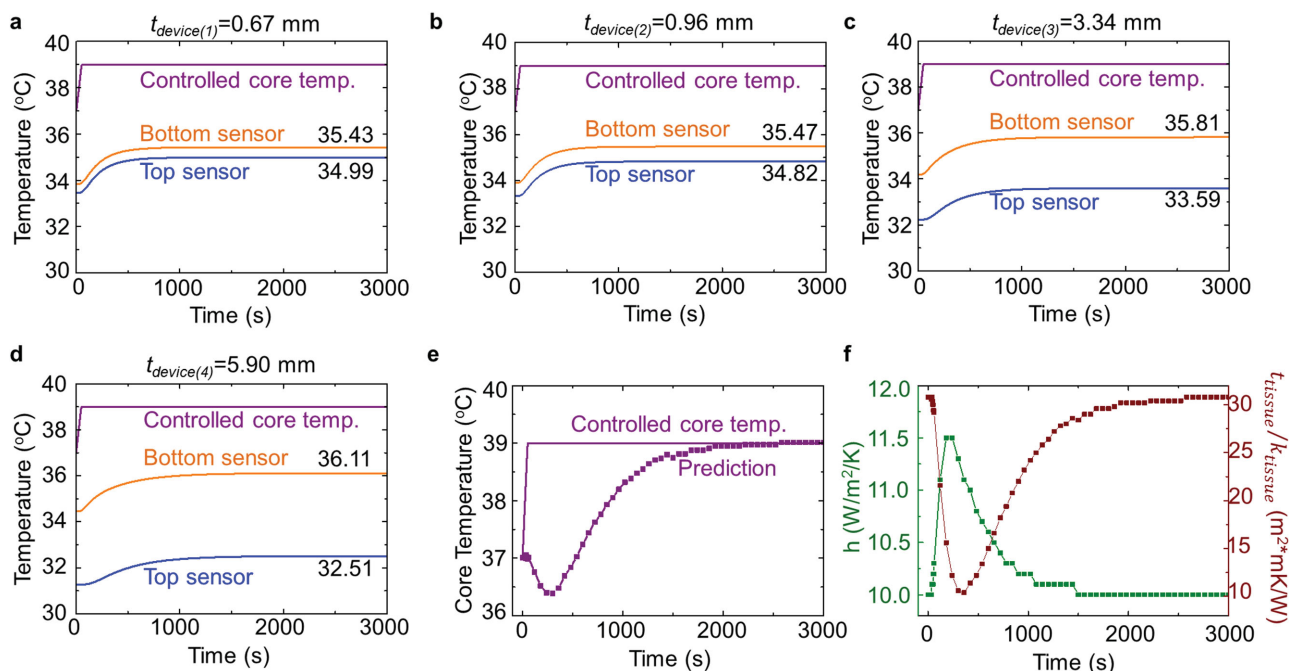


Figure 3. Transient effects in the thermal conduction model. a–d) Temperature history of top and bottom sensors due to an increase in the core body temperature from 37 °C to 39 °C over 50 s, for four devices with $t_{\text{device}} = 0.67, 0.96, 3.34,$ and 5.90 mm . e) Predicted evolution of core body temperature by using the sensor temperatures in (a–d) as inputs. f) Predicted evolution of the convection coefficient and tissue property by using the sensor temperatures in (a–d) as inputs.

To reduce the overall size of the device while ensuring a sufficiently large difference in the temperature of the two sensors, the thickness (t_{device}) should not be too much smaller than the lateral size (s_{device}). In this geometry, 3D thermal conduction can be important and the 1D model may not provide sufficient accuracy. An example appears in **Figure 4a** for a device with a thickness (5.9 mm) that is comparable to the lateral size (20 mm \times 20 mm), under a typical condition (with $T_{\text{room}} = 22\text{ }^{\circ}\text{C}$, $T_{\text{core}} = 37\text{ }^{\circ}\text{C}$, and $h = 10\text{ W K}^{-1}\text{ m}^{-2}$). Here, the side surfaces dissipate heat into the environment such that a temperature gradient can be observed along the sensor plane (normal to the thickness direction). The magnitude of the temperature calculated by the 3D model lies below that of the 1D model (Equations (2) and (3)). In particular, the maximum difference of those two models (1D and 3D) can reach $\approx 4.76\text{ }^{\circ}\text{C}$ at the plane of the top sensor and $\approx 1.93\text{ }^{\circ}\text{C}$ at the plane of the bottom sensor. Both values are significant compared to the difference ($15\text{ }^{\circ}\text{C}$) between T_{core} and T_{room} . To take this 3D effect into account for a moderately thick device (e.g., with the ratio $t_{\text{device}}/s_{\text{device}} < 1/3$), a correction in the convection coefficient can be introduced in the 1D model. The corrected value ($h_{\text{corrected}}$) is given by

$$h_{\text{corrected}} \approx h \left(1 + C \frac{t_{\text{device}} + t_{\text{fabric}}}{s_{\text{device}}} \right) \quad (5)$$

where C is a factor that depends on the location of the sensor, which can be determined through comparison to accurate calculations of 3D FEA with different device thicknesses (e.g., 0.5–6.0 mm) and tissue properties (e.g., k_{tissue} ranging from 0.15 to 0.45 $\text{W m}^{-1}\text{ K}^{-1}$). Minimization of the average error of the temperatures predicted by the corrected model gives the optimized correction factor, e.g., 2.5 and 3.5 (Figure 4b) for the top and bottom sensors (with the location illustrated in Figure S6a, Supporting Information) of the device used in the experiments, as described in the next section. Figure 4c demonstrates that the agreement of the corrected 1D model with 3D FEA results is indeed much better than that of the uncorrected case, for a representative device (3.34 mm in thickness) under different natural convection conditions (with h in the range of 5–30 $\text{W K}^{-1}\text{ m}^{-2}$).

2.4. Experimental Validation of Devices and Modeling Algorithms

Experiments (see the Experimental Section for details) that adopt thermal models of skin and underlying tissue serve to validate the behavior of devices built according to the above approach. A representative experimental setup appears in **Figure 5a**, with four different temperature devices covered by a thin (1.0 mm) layer of fabric and placed on the top of the tissue model. Four sets of experiments were performed using devices with different dimensions (four different thicknesses, 5.9, 3.34, 0.96, and 0.67 mm, for the device with a lateral size of 20 mm \times 20 mm; two different thicknesses, 4.03 and 2.24 mm, for the device with a lateral size of 50 mm \times 50 mm). Additionally, experiments with several different ambient air convection conditions provided indications of performance in varied environments.

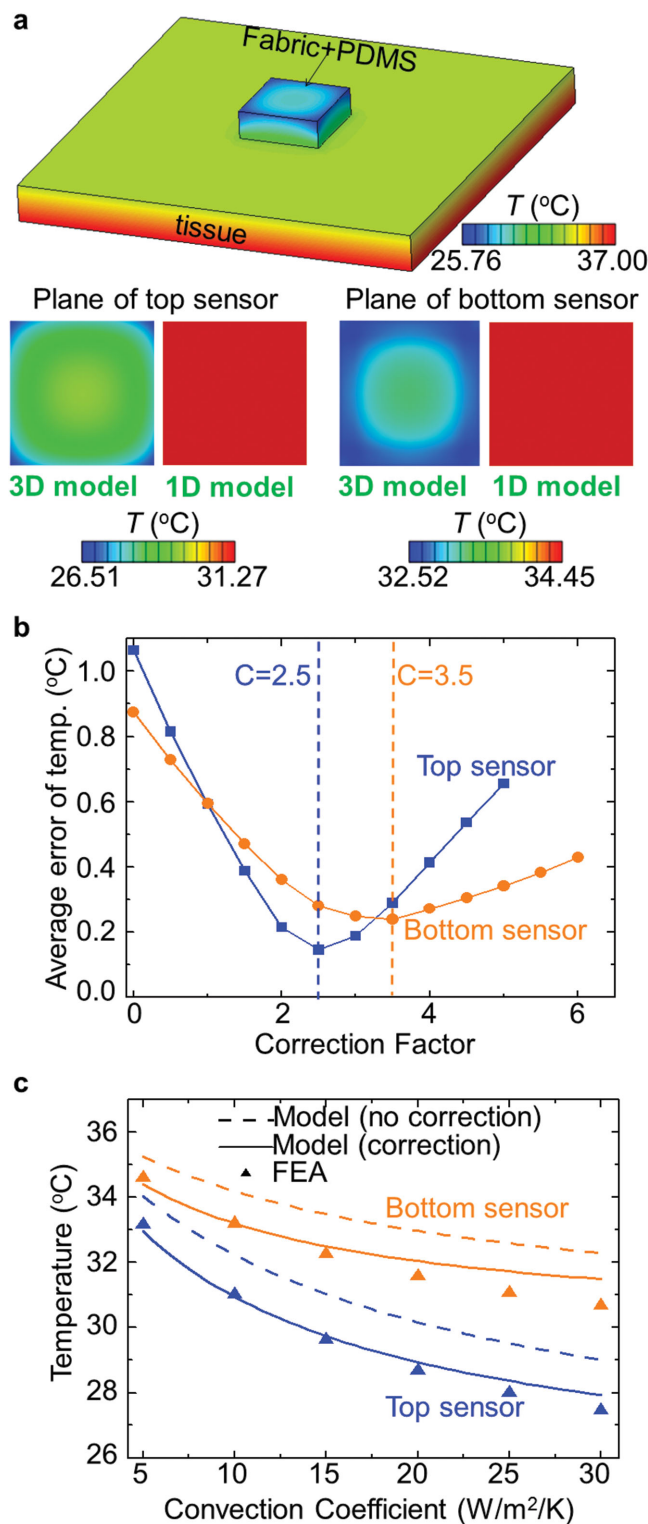


Figure 4. 3D effects in the temperature distribution. a) Temperature distribution of the device and underlying tissue based on calculations by 3D FEA (with $T_{\text{room}} = 22\text{ }^{\circ}\text{C}$, $T_{\text{core}} = 37\text{ }^{\circ}\text{C}$, and $h = 10\text{ W}^{-1}\text{ K}^{-1}\text{ m}^{-2}$), and comparison with results of 1D FEA at the top and bottom planes of the sensors. b) Average error of the temperature prediction based on the corrected model as a function of the correction factor. c) Results of sensor temperature based on FEA and theoretical models for the device with $t_{\text{device}} = 3.34\text{ mm}$.

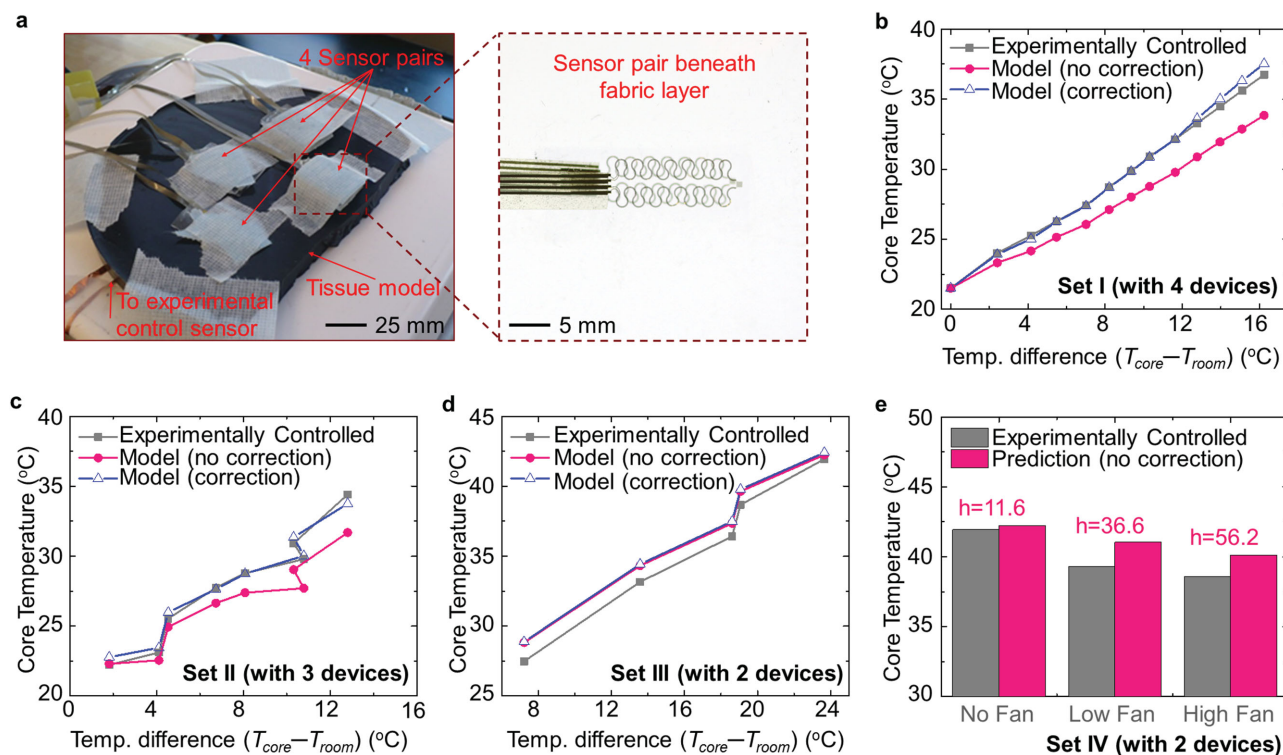


Figure 5. Experiments for validation of the theoretical model. a) Photograph of the experimental setup. Experimentally controlled core body temperature and the model predictions based on the developed algorithm in the (b) first set of experiments with four devices (5.9, 3.34, 0.96, and 0.67 mm) with a lateral size of 20 mm × 20 mm, c) second set of experiments with three devices (5.9, 3.34, and 0.96 mm) with a lateral size of 20 mm × 20 mm, and d) third set of experiments with two devices (4.02 and 2.24 mm) with a lateral size of 50 mm × 50 mm. e) Histogram of model predictions for core body temperature under three different levels of convection conditions using two devices (4.02 and 2.24 mm) with a lateral size of 50 mm × 50 mm.

Figure 5b,c illustrates the crucial roles of 3D thermal conduction in the prediction of core body temperature for relatively thick devices (e.g., 20 mm × 20 mm × 5.9 mm). Here, the uncorrected model induces a considerable deviation from the experimentally controlled values. By contrast, the 3D thermal conduction is almost negligible in the prediction of core body temperature for relatively thin devices (e.g., 50 mm × 50 mm × 4.03 mm or 50 mm × 50 mm × 2.24 mm), as shown by Figure 5d. The correction introduced in Section 2.3 is not necessary in this case, consistent with the small correction factors (0.25 for the top sensor and 0.51 for the bottom sensor, shown in Figure S6b,c, Supporting Information). The results in Figure 5b–d also demonstrate that the use of additional devices improves the accuracy, as evidenced by the average differences (≈ 0.24 °C for four devices, ≈ 0.35 °C for three devices, and ≈ 1.02 °C for two devices) from the experimentally controlled values. Considering the wide range (22–38 °C) of variation in the core body temperature during the experiments and the high sensitivity (≈ 0.02 °C) obtained in Section 2.2, the accuracy of the system with four devices has the potential to satisfy requirements in practical applications. Besides working in natural convection conditions (for the experiments in Figure 5b–d), Figure 5e further shows the utility of the system under accelerated air circulation, adjusted with a fan. The magnitude of the convection coefficient inferred by the algorithm corresponds reasonably well with the convection conditions used in the three different

experiments. All four sets of experiments illustrate the validity of the devices and modeling techniques.

3. Discussion

Besides the strategy of using multiple differential devices with different separation thicknesses, the model developed in Section 2 also indicates the feasibility for an alternative approach in which different separation materials are adopted in multiple devices. Cellular elastomeric materials are particularly attractive for this purpose due to thermal properties (especially the thermal conductivity) that can be tuned by tailoring the void fraction. Furthermore, the ultralow thermal conductivity (e.g., ≈ 0.03 W K⁻¹ m⁻¹) of these materials allows reduced device thicknesses, while achieving a similar level of temperature difference between the two offset sensors. This advantage improves the bendability of the device (Figure S7, Supporting Information) and its permeability. Figure 6a,b provides an example built using polyurethane (PU) foam with a high void fraction ($\approx 93\%$), which allows strong bending deformations (with a bending radius of ≈ 10 mm) as shown in Figure 6c. According to FEA results (Figure 6d) based on transient thermal conduction, the sensors embedded in PU foam (1.0 mm in thickness) have response times (≈ 447 s) that are comparable to those (≈ 505 s) of sensors embedded in silicone (1.0 mm in thickness), while

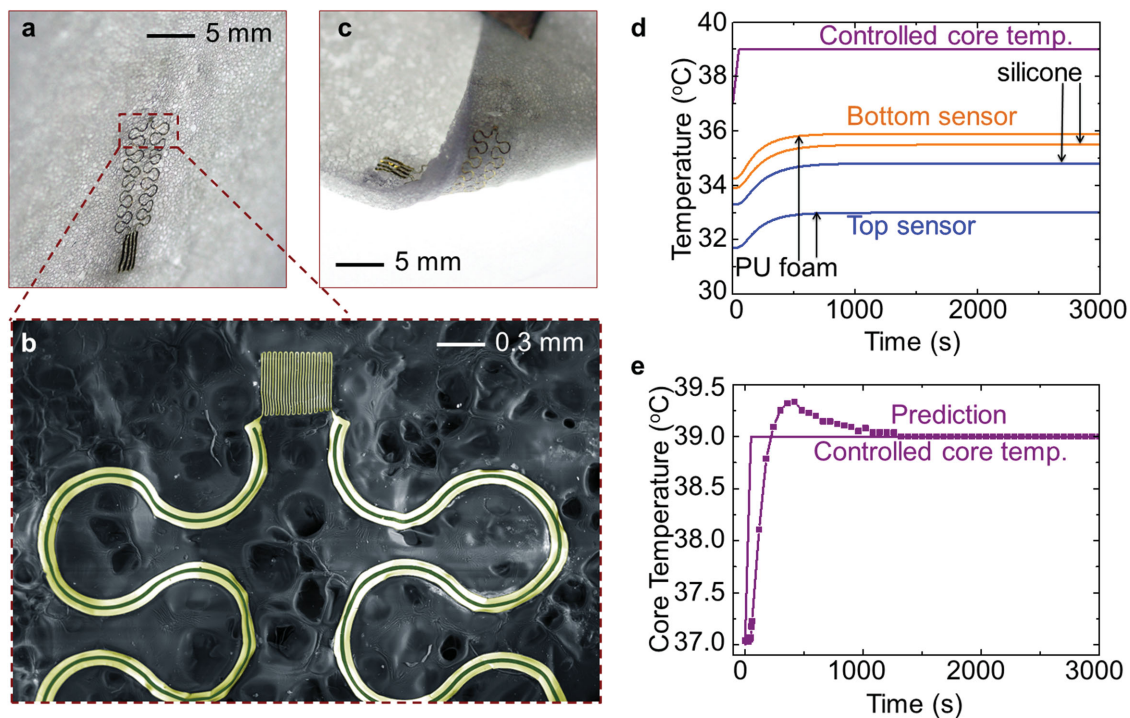


Figure 6. Concepts for tailoring the properties of separation materials for measurement of core body temperature. a) Optical images of a device with polyurethane (PU) foam as the separation material. b) Enlarged view of a temperature sensor. c) Optical image of the device subject to a bending deformation. d) Temperature history of the top and bottom sensors when the core body temperature increases from 37 °C to 39 °C over 50 s, for two devices with the same thickness (1.0 mm) and different separation materials (silicone and PU foam). e) Predicted evolution of the core body temperature using sensor temperatures in (d) as inputs.

providing a relatively large temperature difference (≈ 2.89 °C) in the steady state. A numerical experiment that uses these time-dependent sensor temperatures in the inverse model indicates a short response time (≈ 602 s) for measurement of core body temperature, particularly compared to the system (with a response time of ≈ 1440 s) in Figure 3.

4. Conclusion

This paper presents a systematic study of soft, wearable differential temperature sensors for noninvasive measurements of core body temperature. The content combines analytical, numerical, and experimental approaches. The sensors exploit materials and structural designs that enable conformable integration onto the surface of skin, with the capability of sustaining high levels of deformations in various modes. A theoretical approach that exploits multiple sensors with various separation thicknesses or materials shows promise in the determination of core body temperature. Fundamental investigations on the sensitivity, accuracy, and response time provide important guidelines for future optimization. Four different sets of experiments illustrate the validity of the methods, and verify the expected improvements in accuracy enabled by the use of additional sensors. These outcomes could have potential in long-term, continuous monitoring of core body temperature.

5. Experimental Section

Fabrication of Differential Temperature Sensors: Fabrication began with a 3 in. Si wafer coated with a 200 nm layer of poly(methyl methacrylate) (PMMA 495 A2, Microchem, USA), followed by 1.2 μm of polyimide (PI-2545, HD Microsystems, USA). Photolithographic patterning of a bilayer of Cr (6 nm)/Au (75 nm) deposited by electron beam evaporation defined the sensing/heating elements. A second photolithographic patterning of a metal stack of Ti (10 nm)/Cu (550 nm)/Ti (20 nm)/Au (25 nm) defined the interconnect wires. A second layer of polyimide (1.2 μm) placed the sensing/heating elements in the neutral mechanical plane and provided electrical insulation and mechanical strain isolation. Reactive ion etching of the polyimide defined the mesh layout of the array and exposed the bonding locations. A water-soluble tape (5414, 3M, USA) enabled the removal of the mesh layout from the Si wafer to expose its back surface for deposition of Ti (3 nm)/SiO₂ (30 nm) by electron beam evaporation. Transfer to a thin silicone layer (10 μm , Sylgard 184, Dow Corning, USA) spin-cast onto a glass slide, surface treated to reduce adhesion of the silicone, resulted in the formation of strong bonds due to condensation reactions between exposed hydroxyl groups and the SiO₂ and silicone. Immersion in warm water allowed the removal of the tape. A thin (100 μm), flexible, conductive cable bonded with heat and pressure to contacting pads at the periphery served as a connection to external electronics. Devices were then laminated to each side of the separation material (either Sylgard 184 as seen in Figure 1, or polyurethane foam (FlexFoam-iT! III, Smooth-On, USA), as seen in Figure 6). Finally, a thin layer (40 μm) of adhesive silicone (Silbione RT Gel 4147 A/B, Bluestar Silicones, USA) was applied via a doctor blade to each side of the final differential sensor device.

Experimental Studies: A precision hot plate (Super Nuova, Thermo Scientific, USA) placed in an ambient controlled chamber served as the model of a core temperature heat source. A cranial tissue model

(9.2 mm thickness of Sylgard 170, Dow Corning, USA) laminated to the hot plate provided a thermal resistance structure similar to that expected for an average human skull. A small resistance temperature detector (PTS 1206, Vishay Beyschlag, Germany) embedded between the hot plate and the tissue model recorded the experimentally controlled core temperature. Each differential temperature sensor was laminated to the top surface of the tissue model. Finally, a 1 mm thick fabric layer (two layers of Ease Release Tape, 3M, USA) modeled conditions for practical use. During all experiments, the resistance of each sensor was recorded, in a four-point configuration, by a 22 bit digital multimeter (USB-4065, National Instruments, USA). In order to record data from all sensors during experiments, sensor recordings were time-multiplexed via an external switch matrix (U802, LedgeStone Technologies, USA). Resistance values were converted to temperature values via a prior sensor calibration. Different convection conditions were achieved by applying varied levels of air flow from a blower fan over the experimental setup.

Supporting Information

Supporting Information is available from the Wiley Online Library or from the author.

Acknowledgements

Y.H.Z., R.C.W., and H.Y.L. contributed equally to this work. Y.H. and J.A.R. acknowledge the support from the NSF (DMR-1242240, CMMI-1300846, CMMI-1400169, and DGE-1144245) and the NIH (Grant No. R01EB019337).

Received: February 16, 2015

Revised: March 27, 2015

Published online: May 7, 2015

- [1] C. V. Gisolfi, F. Mora, *The Hot Brain*, The MIT Press, Cambridge 2000.
- [2] C. Childs, K. W. Lunn, *Crit. Care* **2013**, *17*, 222.
- [3] M. Matsumoto, J. Sugama, M. Okuwa, M. Dai, J. Matsuo, H. Sanada, *Arch. Gerontol. Geriatrics* **2013**, *57*, 428.
- [4] C. Byrne, C. L. Lim, *Br. J. Sports Med.* **2007**, *41*, 126.
- [5] M. W. Tabor, D. M. Blaho, W. R. Schriver, *Oral Surg. Oral Med. Oral Pathol.* **1981**, *51*, 581.
- [6] P. A. Chapon, N. Bessot, A. Gauthier, S. Besnard, S. Moussay, *J. Therm. Biol.* **2012**, *37*, 255.
- [7] W. J. Kort, J. M. Hekking-Weijma, M. T. TenKate, V. Sorm, R. VanStrik, *Lab. Animals* **1998**, *32*, 260.
- [8] R. H. Fox, A. J. Solman, R. Isaacs, A. J. Fry, I. C. MacDonald, *Clin. Sci.* **1973**, *44*, 81.
- [9] T. Kobayashi, T. Nemoto, A. Kamiya, T. Togawa, *Ann. Biomed. Eng.* **1975**, *3*, 181.
- [10] A. Zeiner, J. Klewer, F. Sterz, M. Haugk, D. Krizanac, C. Testori, H. Losert, S. Ayati, M. Holzer, *Resuscitation* **2010**, *81*, 861.
- [11] L. P. J. Teunissen, J. Klewer, A. de Haan, J. J. de Koning, H. A. M. Daanen, *Physiol. Meas.* **2011**, *32*, 559.
- [12] K. I. Kitamura, X. Zhu, W. X. Chen, T. Nemoto, *Med. Eng. Phys.* **2010**, *32*, 1.
- [13] S. Y. Sim, W. K. Lee, H. J. Baek, K. S. Park, A noninvasive temperature measuring system for estimating deep body temperature in bed, in 34th Annu. Int. Conf. IEEE Engineering-in-Medicine-and-Biology-Society (EMBS), San Diego, CA **2012**, p. 3460.
- [14] M. Yamakage, A. Namiki, *J. Anesthesia* **2003**, *17*, 108.
- [15] N. Bowden, S. Brittain, A. G. Evans, J. W. Hutchinson, G. M. Whitesides, *Nature* **1998**, *393*, 146.
- [16] T. Li, Z. G. Suo, S. P. Lacour, S. Wagner, *J. Mater. Res.* **2005**, *20*, 3274.
- [17] D. H. Kim, J. Z. Song, W. M. Choi, H. S. Kim, R. H. Kim, Z. J. Liu, Y. Y. Huang, K. C. Hwang, Y. W. Zhang, J. A. Rogers, *Proc. Natl. Acad. Sci. U.S.A.* **2008**, *105*, 18675.
- [18] D. H. Kim, N. S. Lu, R. Ma, Y. S. Kim, R. H. Kim, S. D. Wang, J. Wu, S. M. Won, H. Tao, A. Islam, K. J. Yu, T. I. Kim, R. Chowdhury, M. Ying, L. Z. Xu, M. Li, H. J. Chung, H. Keum, M. McCormick, P. Liu, Y. W. Zhang, F. G. Omenetto, Y. G. Huang, T. Coleman, J. A. Rogers, *Science* **2011**, *333*, 838.
- [19] Z. G. Suo, *MRS Bull.* **2012**, *37*, 218.
- [20] J. Vanfleteren, M. Gonzalez, F. Bossuyt, Y. Y. Hsu, T. Vervust, I. De Wolf, M. Jablonski, *MRS Bull.* **2012**, *37*, 254.
- [21] S. Wagner, S. Bauer, *MRS Bull.* **2012**, *37*, 207.
- [22] S. Xu, Y. H. Zhang, J. Cho, J. Lee, X. Huang, L. Jia, J. A. Fan, Y. W. Su, J. Su, H. G. Zhang, H. Y. Cheng, B. W. Lu, C. J. Yu, C. Chuang, T. I. Kim, T. Song, K. Shigeta, S. Kang, C. Dagdeviren, I. Petrov, P. V. Braun, Y. Huang, U. Paik, J. A. Rogers, *Nat. Commun.* **2013**, *4*, 1543.
- [23] Y. H. Zhang, S. Xu, H. R. Fu, J. Lee, J. Su, K. C. Hwang, J. A. Rogers, Y. Huang, *Soft Matter* **2013**, *9*, 8062.
- [24] D. Son, J. Lee, S. Qiao, R. Ghaffari, J. Kim, J. E. Lee, C. Song, S. J. Kim, D. J. Lee, S. W. Jun, S. Yang, M. Park, J. Shin, K. Do, M. Lee, K. Kang, C. S. Hwang, N. S. Lu, T. Hyeon, D. H. Kim, *Nat. Nanotechnol.* **2014**, *9*, 397.
- [25] D. J. Lipomi, M. Vosgueritchian, B. C. K. Tee, S. L. Hellstrom, J. A. Lee, C. H. Fox, Z. N. Bao, *Nat. Nanotechnol.* **2011**, *6*, 788.
- [26] S. C. B. Mannsfeld, B. C. K. Tee, R. M. Stoltenberg, C. Chen, S. Barman, B. V. O. Muir, A. N. Sokolov, C. Reese, Z. N. Bao, *Nat. Mater.* **2010**, *9*, 859.
- [27] G. Schwartz, B. C. K. Tee, J. G. Mei, A. L. Appleton, D. H. Kim, H. L. Wang, Z. N. Bao, *Nat. Commun.* **2013**, *4*, 1859.
- [28] S. Xu, Y. H. Zhang, L. Jia, K. E. Mathewson, K. I. Jang, J. Kim, H. R. Fu, X. Huang, P. Chava, R. H. Wang, S. Bhole, L. Z. Wang, Y. J. Na, Y. Guan, M. Flavin, Z. S. Han, Y. G. Huang, J. A. Rogers, *Science* **2014**, *344*, 70.
- [29] M. Kaltenbrunner, T. Sekitani, J. Reeder, T. Yokota, K. Kuribara, T. Tokuhara, M. Drack, R. Schwodiauer, I. Graz, S. Bauer-Gogonea, S. Bauer, T. Someya, *Nature* **2013**, *499*, 458.
- [30] M. Kaltenbrunner, M. S. White, E. D. Glowacki, T. Sekitani, T. Someya, N. S. Sariciftci, S. Bauer, *Nat. Commun.* **2012**, *3*, 770.
- [31] M. S. White, M. Kaltenbrunner, E. D. Glowacki, K. Gutnichenko, G. Kettlgruber, I. Graz, S. Aazou, C. Ulbricht, D. A. M. Egbe, M. C. Miron, Z. Major, M. C. Scharber, T. Sekitani, T. Someya, S. Bauer, N. S. Sariciftci, *Nat. Photonics* **2013**, *7*, 811.
- [32] D. H. Kim, N. S. Lu, R. Ghaffari, Y. S. Kim, S. P. Lee, L. Z. Xu, J. A. Wu, R. H. Kim, J. Z. Song, Z. J. Liu, J. Viventi, B. de Graff, B. Elolampi, M. Mansour, M. J. Slepian, S. Hwang, J. D. Moss, S. M. Won, Y. G. Huang, B. Litt, J. A. Rogers, *Nat. Mater.* **2011**, *10*, 316.
- [33] C. J. Yu, C. Masarapu, J. P. Rong, B. Q. Wei, H. Q. Jiang, *Adv. Mater.* **2009**, *21*, 4793.
- [34] Y. H. Zhang, H. R. Fu, S. Xu, J. A. Fan, K. C. Hwang, J. Q. Jiang, J. A. Rogers, Y. G. Huang, *J. Mech. Phys. Solids* **2014**, *72*, 115.
- [35] R. C. Webb, A. P. Bonifas, A. Behnaz, Y. H. Zhang, K. J. Yu, H. Y. Cheng, M. X. Shi, Z. G. Bian, Z. J. Liu, Y. S. Kim, W. H. Yeo, J. S. Park, J. Z. Song, Y. H. Li, Y. G. Huang, A. M. Gorbach, J. A. Rogers, *Nat. Mater.* **2013**, *12*, 938.